Construction of ZnFe$_2$O$_4$/g-C$_3$N$_4$ heterojunction as reusable visible-light photocatalyst and the boosted photocatalytic efficiency by photo-self-Fenton effect for organic pollutant degradation

Xiang Li[1], Hongna Xing[1], Xianfeng Yang[1], Dan Wang[1], Juan Feng[1,*], Yan Zong[1], Xiuhong Zhu[1,*] , Xinghua Li[1], and Xinliang Zheng[1]

[1] *School of Physics, State Key Laboratory of Photon-Technology in Western China Energy, Northwest University, Xi'an 710127, China*

ABSTRACT

Designing reusable visible-light photocatalysts and understanding the catalytic mechanism are of great significance in environmental remediation. Herein, ZnFe$_2$O$_4$/g-C$_3$N$_4$ heterojunctions were constructed by decorating g-C$_3$N$_4$ nanosheets with tiny ZnFe$_2$O$_4$ nanoparticles, and their photocatalytic activity, recyclability and degradation mechanism were investigated. Compared to the onefold g-C$_3$N$_4$ or ZnFe$_2$O$_4$, the ZnFe$_2$O$_4$/g-C$_3$N$_4$ heterojunction shows boosted photocatalytic activities for degradation of three different dyes. The heterojunction construction can greatly improve the visible-light absorption capacity and photo-induced electron–hole separation, resulting in boosted photocatalytic activities. The ultrathin layered g-C$_3$N$_4$ nanosheets and tiny ZnFe$_2$O$_4$ nanoparticles in heterojunction can sufficiently contact with each other, which can improve the specific surface area, provide abundant active sites and enhance the photocatalytic efficiency. The degradation efficiencies of ZnFe$_2$O$_4$/g-C$_3$N$_4$ heterojunction are 96.27% for Methylene Blue (MB), 73.17% for Methyl Orange (MO) and 92.4% for Rhodamine B (RhB). The corresponding kinetic constant of ZnFe$_2$O$_4$/g-C$_3$N$_4$ are 0.019, 0.007 and 0.015 min^{-1}, which are nearly 2.4, 3.5 and 1.7 times higher than that of the single g-C$_3$N$_4$, respectively. The capacity of MB by ZnFe$_2$O$_4$/g-C$_3$N$_4$ remains 88.09% after four cycles. Free radical trapping experiment demonstrates that the ZnFe$_2$O$_4$/g-C$_3$N$_4$ heterojunction is a photo-self-Fenton system, which can spontaneously produce H$_2$O$_2$, resulting in the formation of ·OH radicals during the photocatalytic process. The synergistic effect of ·OH and ·O$_2^-$ radicals is responsible for degradation organic pollutants. In addition, the ZnFe$_2$O$_4$/g-C$_3$N$_4$ heterojunction photocatalysts can be easily separated by an applied magnet, behaving reused capacity.

Address correspondence to E-mail: fjuan5479@nwu.edu.cn; zhuxh@nwu.edu.cn

 Springer

1 Introduction

The emission of various non-biodegradable and persistent pollutants in industrial processes and household wastewater pose a serious threat to the ecological environment and human health [1–4]. Researchers have adopted various methods to solve the above problems. Among them, homogeneous Fenton reaction or heterogeneous sulfate radicals based advanced oxidation processes (AOPs) have been widely applied in eliminating the organic pollutants through the efficient generation of reactive oxygen species (e.g., $\cdot OH$, $\cdot SO_4^-$ and singlet oxygen ($^1O_2$), etc.) [5, 6]. However, the degradation efficiency is usually limited by the following aspects: (1) The sluggish regeneration (Fe^{3+} to Fe^{2+}) and narrow pH adaptability limit the practical applications of homogeneous Fenton reaction. Previous studies show that the oxyhydroxides is formed by co-precipitation of Fe^{3+} and Fe^{2+} at pH > 3 [7]; (2) Additional hydrogen peroxide (H_2O_2) or persulfates (peroxymonosulfate (PMS) and peroxydisulfate (PDS)) are required [8, 9]. The H_2O_2 solution is a typical hazardous chemical, and persulfates have strong oxidation property. They all may pose a risk of secondary environmental pollution; (3) The utilization and activation efficiency of H_2O_2 and persulfates are usually low [10, 11]. Nowadays, many efforts focus on improving the degradation efficiency by improving Fenton reaction, which can be realized by adding cocatalysts (such as carbon materials, non-metallic elements) or using external techniques (including UV, ultrasound or heat) [12–16]. However, some problems still exist, such as the toxicity, instability, high cost and complex preparation process. Therefore, an efficient, affordable and environmentally friendly treatment approach is urgently desired.

Graphite carbon nitride (g-C_3N_4), as a metal-free polymeric photocatalyst, has earned increasing attention because of its non-toxicity, suitable electronic band gap (ca. 2.7 eV) and reliable stability [17–19]. However, the limited visible light absorption and rapid complexation efficiency of photogenerated electron–hole pairs significantly restrict the applications of g-C_3N_4 [20]. Constructing heterostructures is an effective strategy, in which g-C_3N_4 was coupled by other semiconductors with suitable band structure [21]. The heterojunction structures can effectively enhance the separation efficiency of photogenerated charge carriers, broaden the visible-light absorption range and improve the photocatalytic activity. Besides, for practical applications, the separation of catalyst without loss during the recycling process is also an important hotspot to be considered [22].

Zinc ferrite ($ZnFe_2O_4$) has attracted widespread attention in photocatalysis due to its broad visible spectrum, narrow band gap (ca. 1.9 eV), magnetic recyclability and photochemical stability [23, 24]. Doped zinc ferrite and zinc ferrite-based heterojunctions have been constructed for photocatalytic applications [25–28]. Coupling g-C_3N_4 nanosheets with magnetic $ZnFe_2O_4$ nanoparticles can overcome several drawbacks of g-C_3N_4 monomer, such as low recycle ability, fast photogenic charge carriers recombination, poor redox ability and so on [29, 30]. Researchers have reported that the $ZnFe_2O_4$/g-C_3N_4 heterojunction shows high photocatalytic degradation activity under visible light irradiation, during which H_2O_2 was added to induce photo-Fenton reaction [31, 32]. The addition of $ZnFe_2O_4$ can accelerate the electron–hole separation and migration efficiency. However, a careful study and analysis is still required to answer these questions: (1) whether additive H_2O_2 is prerequisite during the photocatalytic process; (2) the relationship between H_2O_2 concentration and catalytic efficiency; (3) the generation path of free radicals; (4) the mechanism of improved photocatalytic performance.

Herein, magnetic $ZnFe_2O_4$/g-C_3N_4 heterojunctions with different $ZnFe_2O_4$ contents were constructed as reusable visible-light photocatalysts. The g-C_3N_4 component promotes the spontaneous production of H_2O_2, inducing photo-self-Fenton reaction for boosting the photocatalytic performance, that can overcome the shortcomings of traditional Fenton technology during which additional H_2O_2 is needed. Furthermore, the generation path of free radicals and photo-self-Fenton enhanced photocatalytic mechanism are systematically studied. This work not only provide a method for the design of magnetic g-C_3N_4 based heterojunctions as reusable visible-light photocatalysts, but also gives a new sight to enhance the photocatalytic efficiency through photo-self-Fenton reaction.

2 Experiments

2.1 Synthesis of $ZnFe_2O_4$/g-C_3N_4 heterojunctions

g-C_3N_4 nanosheets and $ZnFe_2O_4$ nanoparticles were prepared by calcination process and solvothermal method, respectively. The detailed experiments are shown in the supporting information. $ZnFe_2O_4$/g-C_3N_4 heterojunctions were synthesized by a reflux route. In a typical process, 200 mg g-C_3N_4 was dispersed into 60 mL EG by ultrasonic treatment for 1 h. Then 20 mg $ZnFe_2O_4$ nanoparticles were dissolved in the g-C_3N_4-containing solution, followed by ultrasonic treatment for another 1 h. Finally, the mixture solution was refluxed at 200 °C for 2 h under magnetic stirring. The obtained $ZnFe_2O_4$/g-C_3N_4 heterojunctions were centrifuged at 10,000 rpm, and washed with water and ethanol for several times. The products were dried at 60 °C in air. By changing the $ZnFe_2O_4$ content to be 5, 10, 20, 30 and 40 mg, the samples were named as ZFO/CN-X (X = 5, 10, 20, 30 and 40). The materials and characterizations can be seen in the supporting information.

2.2 Photocatalytic activity evaluation

The photocatalytic activity of $ZnFe_2O_4$/g-C_3N_4 heterojunctions was evaluated by photodegradation of methylene blue (MB) under visible light irradiation (300 W Xenon lamp with a cut-off filter of 420 nm) in a photocatalytic reactor. 50 mg of the $ZnFe_2O_4$/g-C_3N_4 heterojunctions were dispersed in 50 mL of MB (20 ppm) water solution. Prior to the light irradiation, the suspension of mixtures were agitated in dark for 30 min. The suspension solutions were exposed under visible light irradiation for 180 min. 3 mL aliquots of the reaction mixture suspensions were taken at certain intervals, and subjected to centrifugation to remove the $ZnFe_2O_4$/g-C_3N_4 heterojunction photocatalysts from the filtrate. The clear solution containing MB were analyzed by UV–vis spectrophotometer at an absorbance of 664 nm.

2.3 Detection experiment of H_2O_2

The concentration of H_2O_2 produced during photocatalysis was determined by iodometry. The detection experiment of H_2O_2 is consistent with the photocatalytic experiment (Sect. 2.2) without MB.

50 mL water solution containing 50 mg $ZnFe_2O_4$/g-C_3N_4 heterojunctions were exposed under visible light irradiation for 180 min. At certain intervals, 3 mL aliquots were taken, and centrifuged to remove the $ZnFe_2O_4$/g-C_3N_4 heterojunction photocatalysts. Then, 1 mL potassium hydrogen phthalate ($C_8H_5KO_4$) aqueous solution (0.1 M) and 1 mL potassium iodide (KI) aqueous solution (0.4 M) were added to the above 3 mL solution, and kept for 30 min. $C_8H_5KO_4$ and KI are used to provide hydrogen ion (H^+) and iodide ion (I^-), respectively. Under acidic condition, the H_2O_2 molecules react with I^-, generating I_3^- ($H_2O_2 + 3I^- + 3H^+ \rightarrow I_3^- + 2H_2O$). The amount of I_3^- was measured by UV–vis spectrometer at its characteristic absorbance peak (350 nm), and then the amount of H_2O_2 generated in the reaction was obtained.

3 Results and discussion

3.1 Characterization of as-prepared photocatalysts

Figure 1a schematically illustrates the fabrication process of $ZnFe_2O_4$/g-C_3N_4 (ZFO/CN) heterojunctions. g-C_3N_4 nanosheets and $ZnFe_2O_4$ nanoparticles were prepared by calcination process and solvothermal method, respectively. Then ZFO/CN heterojunctions were obtained by a refluxed route. Figure 1b shows the XRD patterns of g-C_3N_4 nanosheets, $ZnFe_2O_4$ nanoparticles and ZFO/CN heterojunctions with different amount of $ZnFe_2O_4$ nanoparticles. The bare g-C_3N_4 nanosheets show two characteristic peaks at about 13.01° and 27.45°, belonging to the (100) and (002) crystalline planes, which were related to the in-plane structure of tri-s-triazine units and the interlayer stacking reflection of conjugated aromatic segments, respectively [33, 34]. For the $ZnFe_2O_4$ nanoparticles, the diffraction peaks at 18.18°, 29.91°, 35.23°, 42.82°, 53.11°, 56.61° and 62.15° are attributed to the (111), (220), (222), (400), (422), (511) and (440) planes of cubic $ZnFe_2O_4$ (JCPDS No. 82-1049). The characteristic peaks of both $ZnFe_2O_4$ and g-C_3N_4 can be observed in the ZFO/CN heterojunctions without other impurity phases. This indicates that ZFO/CN heterojunctions were successfully synthesized.

Figure 1c shows the typical FTIR spectra of g-C_3N_4 nanosheets, $ZnFe_2O_4$ nanoparticles and ZFO/CN-20. For the pure g-C_3N_4 nanosheets, the broad absorption
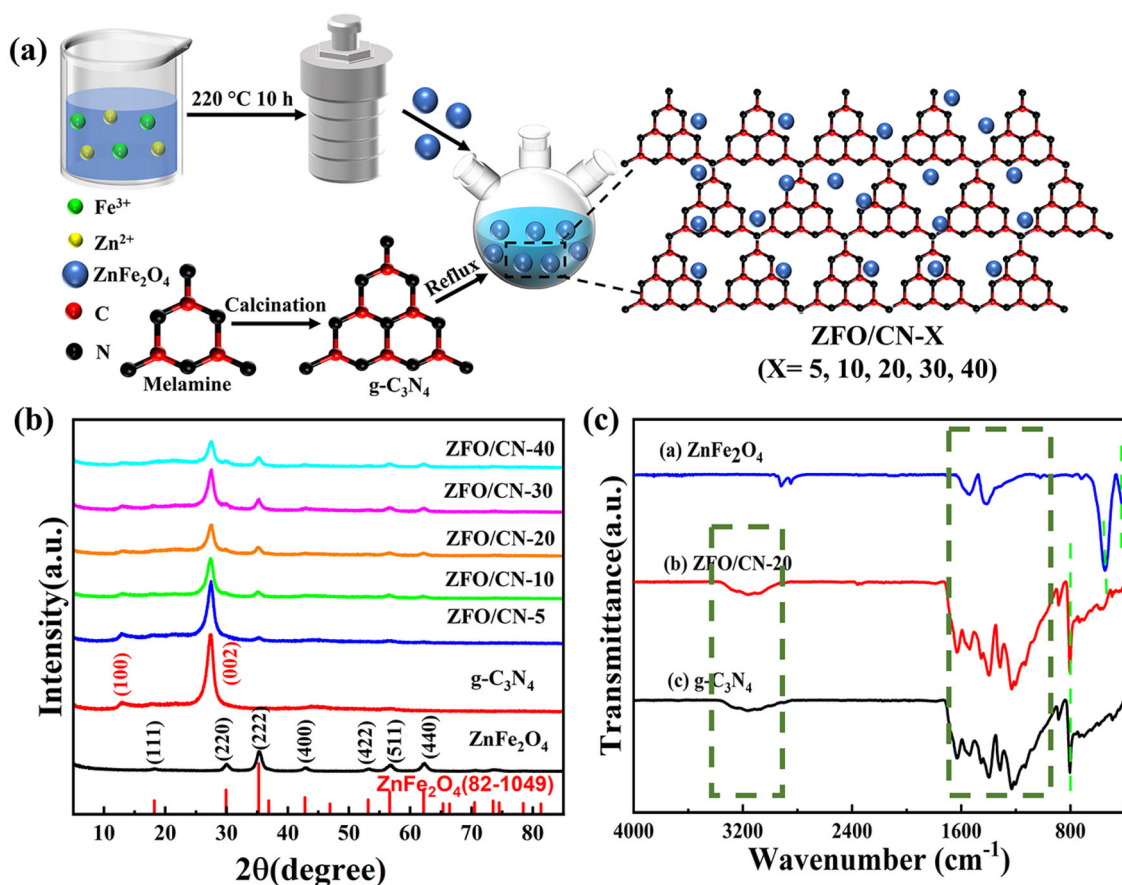
Fig. 1 **a** Schematic illustration of the preparation of $ZnFe_2O_4$/g-C_3N_4 heterojunctions; **b** XRD patterns and **c** FTIR spectra of g-C_3N_4 nanosheets, $ZnFe_2O_4$ nanoparticles and $ZnFe_2O_4$/g-C_3N_4 heterojunction photocatalysts

bands from 3000 to 3400 cm^{-1} is attributed to the –NH stretching vibration modes and –OH of surface adsorbed hydroxyl species. A series of characteristic peaks located in the region of 1200–1600 cm^{-1} are due to the typical stretching vibration of C–N and C=N bonds (heterocycle) in the tri-s-triazine units of g-C_3N_4. The characteristic peak at 805 cm^{-1} is observed for pristine g-C_3N_4, which is related to the bending vibration of tri-s-triazine units [35–37]. The stretching vibrations of Zn–O and Fe–O modes for $ZnFe_2O_4$ are observed at 547 and 423 cm^{-1} [24, 38]. The band positioned at 1636 cm^{-1} signifies the O–H bending vibration of surface adsorbed hydroxyl group. No significant differences are observed between g-C_3N_4 and ZFO/CN-20, suggesting that the addition of $ZnFe_2O_4$ didn't change the chemical structure of g-C_3N_4.

TEM image (Fig. 2a) and AFM image (Fig. 2b) of g-C_3N_4 suggest the two-dimensional sheet-like structure with micro size. The thickness is measured to be about 3.3 nm (Inset of Fig. 2b). The interlayer

spacing of g-C_3N_4 is 0.36 nm [39], indicating that the g-C_3N_4 nanosheets are about nine molecular layers in thickness. TEM image of $ZnFe_2O_4$ nanoparticles (Fig. S1) reveals that the particles are well-distributed with an average diameter of approximately 8.4 nm. Figure S2 shows the SEM image of g-C_3N_4 sheets and $ZnFe_2O_4$/g-C_3N_4 heterojunction photocatalysts with different amounts of $ZnFe_2O_4$. Obviously, the $ZnFe_2O_4$ nanoparticles are uniformly deposited on the surface of g-C_3N_4 sheets, which increases by increasing the $ZnFe_2O_4$ contents. We consider that the EG solvent with multiple hydroxyl functional groups plays an important role during the formation of heterojunctions. During the reflux process, $ZnFe_2O_4$ nanoparticles were surrounded by EG molecules with multiple hydroxyl groups, which can anchor on the surface of g-C_3N_4 nanosheets. Besides, EG is relatively viscous, which can improve the dispersity of $ZnFe_2O_4$ nanoparticles and g-C_3N_4 nanosheets. The good contact recombination is conducive to constructing heterojunction, which is beneficial to
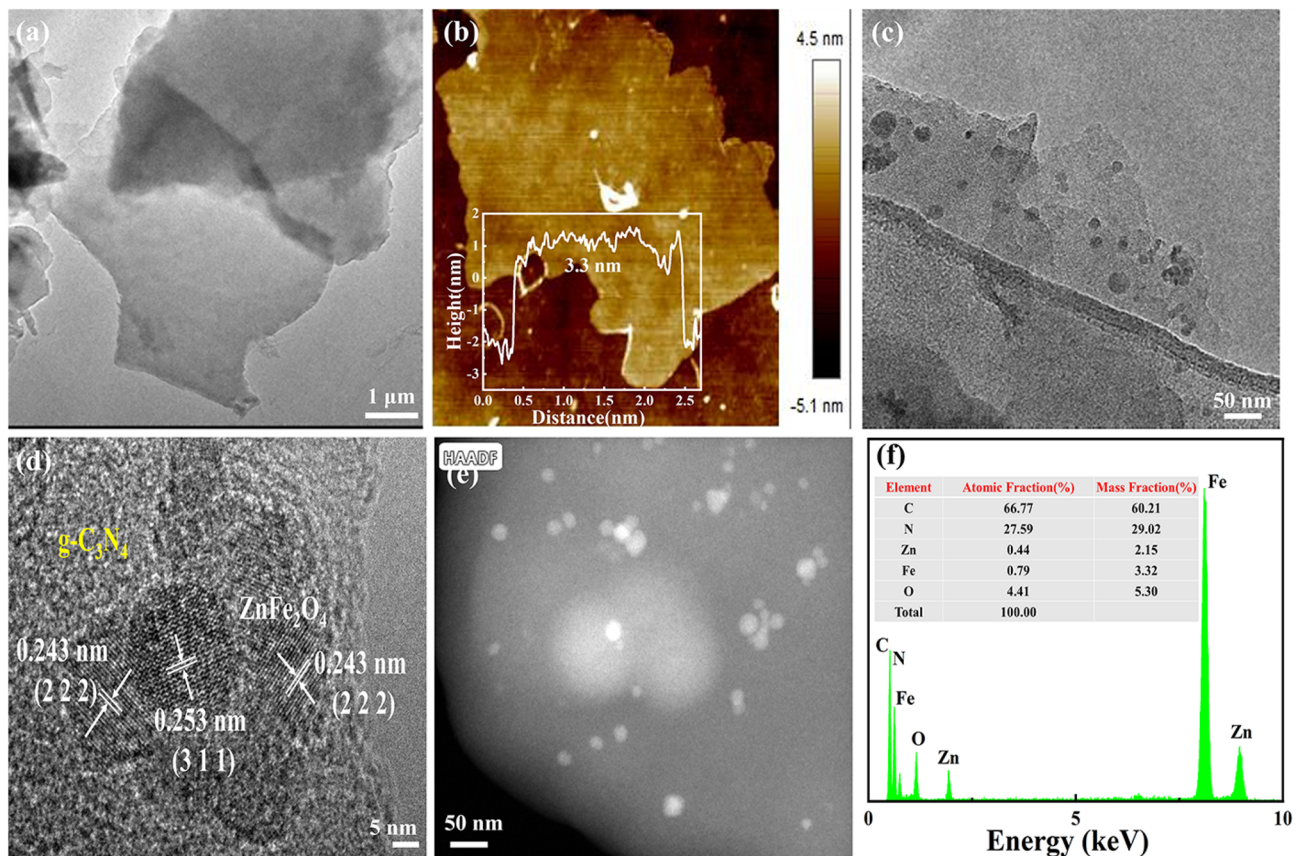
Fig. 2 a TEM image and **b** AFM image of g-C$_3$N$_4$ nanosheets; **c** TEM image, **d** HRTEM image, **e** STEM image and **f** EDS spectrum of ZFO/CN-20 heterojunction

improve the photocatalytic performance of monomer g-C$_3$N$_4$. The typical TEM image (Fig. 2c) and STEM image (Fig. 2e) of ZFO/CN-20 further suggest that tiny ZnFe$_2$O$_4$ nanoparticles are uniformly anchored on the g-C$_3$N$_4$ nanosheets. HRTEM image (Fig. 2d) shows that the lattice spacing distances are 0.243 and 0.253 nm, which are ascribed to the (222) and (311) planes of ZnFe$_2$O$_4$. EDS spectrum of ZFO/CN-20 (Fig. 2f) revealed the existence of C, N, Zn, Fe and O elements in the heterostructure without other element, indicating that the composites are of high purity.

XPS technique was performed to study the surface functional groups and electronic environment of elements in the samples, as shown in Fig. 3. The survey XPS spectra of g-C$_3$N$_4$, ZnFe$_2$O$_4$ and ZFO/CN-20 (Fig. 3a) indicate that C, N, Zn, Fe and O as existed in the ZFO/CN, which is accordant with the XRD data and EDS analysis. The C 1s spectrum of g-C$_3$N$_4$ nanosheets (Down in Fig. 3b) can be fitted into two peaks at about 284.8 and 288.2 eV, which are

attributed to C–C/C=C and N–C=N in g-C$_3$N$_4$ lattice, respectively [40]. In comparison, an additional peak at 285.6 eV can be found in ZFO/CN-20, corresponding to the C=O groups. The presence of C=O groups suggest that ZnFe$_2$O$_4$ nanoparticles are chemically bonded on the surface of g-C$_3$N$_4$ nanosheets in the heterojunction. N 1s spectra of both g-C$_3$N$_4$ and ZFO/CN-20 (Fig. 3c) can be fitted by four peaks, about 398.7 and 399.3 eV for the C=N–C involved in triazine rings and the tri-coordinated N-(C)$_3$, about 400.8 eV for amino groups (C–N–H), and about 404.6 eV for the typical π-excitation in the N–C heterocycles [39]. The Zn 2p spectra of ZnFe$_2$O$_4$ nanoparticles and ZFO/CN-20 (Fig. 3d) show two peaks at about 1021.2 and 1044.4 eV, associated to the Zn 2p$_{3/2}$ and Zn 2p$_{1/2}$ of Zn^{2+}, respectively. Figure 3e shows the Fe 2p spectra. The Fe 2p$_{3/2}$ peak can be fitted into two peaks at about 710.6 and 712.8 eV, which are attributed to the Fe^{3+} in octahedral and tetrahedral sites, respectively. The peak located at about 724.85 eV is attributed to Fe 2p$_{1/2}$ of spinel
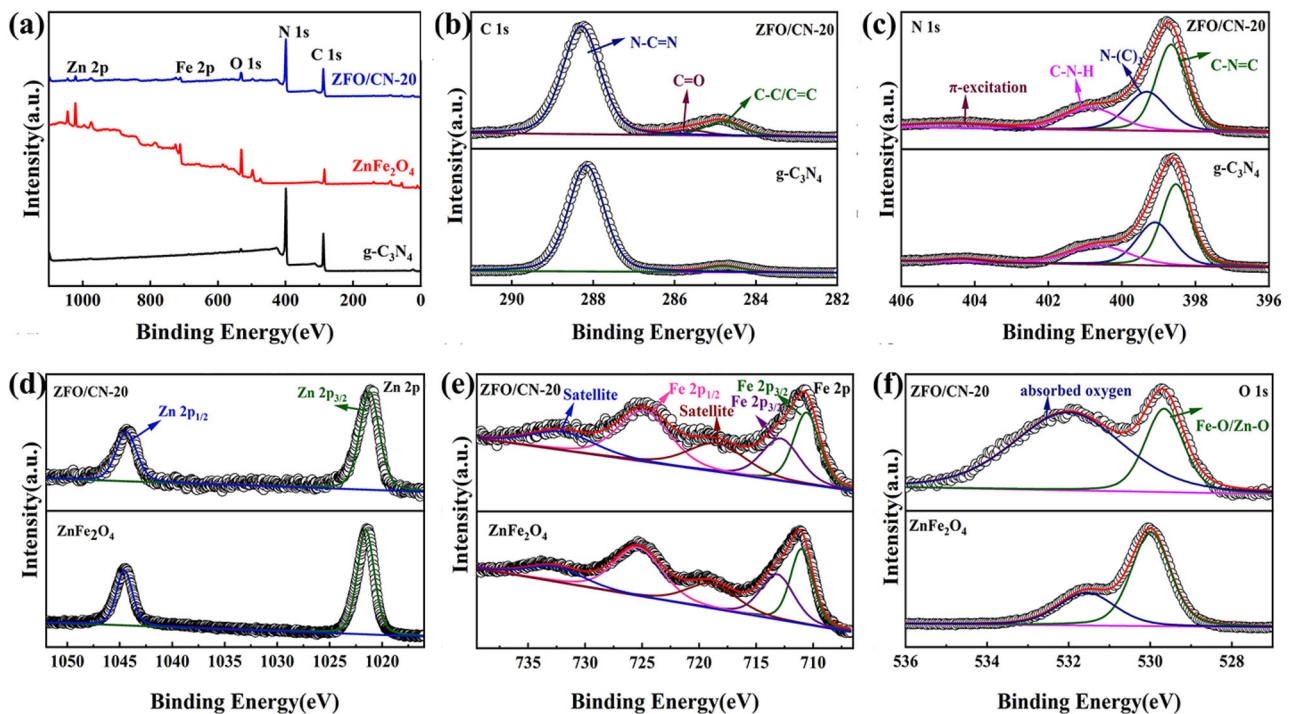
Fig. 3 **a** Survey XPS spectra of g-C_3N_4 nanosheets, $ZnFe_2O_4$ nanoparticles and ZFO/CN-20; **b** C 1s and **c** N 1s spectra of g-C_3N_4 and ZFO/CN-20; **d** Zn 2p, **e** Fe 2p and **f** O 1s spectra of $ZnFe_2O_4$ and ZFO/CN-20

$ZnFe_2O_4$. The other peaks at about 718.5 and 732.0 eV are identified as the shake-up satellite structure. Compared to bare $ZnFe_2O_4$, the satellite peaks of Fe 2p in ZFO/CN-20 composite are slightly shift to lower binding energy, which suggests that defects may exist in the heterojunction. In the O 1s spectra (Fig. 3f), the broad curve exhibit two fitting peaks located at about 529.6 and 532.0 eV, ascribed to the lattice oxygen (denoted as Fe–O and Zn–O) and surface absorbed oxygen species (such as H_2O), respectively [40–42]. The peak parameters of g-C_3N_4, $ZnFe_2O_4$ and ZFO/CN-20 are summarized in Table S2. Compared with binding energies of monomers ($ZnFe_2O_4$ or g-C_3N_4), the binding energies of C 1s and N 1s of ZFO/CN-20 slightly shift toward higher values, while the binding energies of Zn 2p and Fe 2p shift toward lower values. The shift to higher binding energy suggests the elements lose electrons, while the shift to lower binding energy suggests the elements get electrons [27, 43]. The opposite shift indicate that the electron transfer from g-C_3N_4 nanosheets to $ZnFe_2O_4$ nanoparticles at the interface of ZFO/CN heterojunction, which is beneficial for the electron migration during photocatalytic process.

Specific surface area is also an important factor that can affect the photocatalytic activity. Figure S3 shows the N_2 adsorption–desorption isotherms and pore size distribution curves of g-C_3N_4 nanosheets, $ZnFe_2O_4$ nanoparticles and ZFO/CN-20. The isotherms of both bare g-C_3N_4 nanosheets and ZFO/CN-20 show the similar shape with classical type IV, indicating the mesoporous structure [44]. The BET specific surface area, pore diameter and pore volume of the three samples are summarized in Table S1. ZFO/CN-20 reveals the highest specific surface area, about 1.7 times larger than g-C_3N_4 nanosheets. The enhanced specific surface area of ZFO/CN-20 is probably due to that the anchoring tiny $ZnFe_2O_4$ nanoparticles can avert the aggregation of g-C_3N_4 nanosheets. Large specific surface areas could provide abundant active reaction sites and facilitate the adsorption of pollutant molecules [44, 45].

3.2 Optical and photoelectrochemical properties

The photocatalytic activity is affected by the optical absorption performance. Figure 4a displays the UV–vis absorption spectra of g-C_3N_4 nanosheets, $ZnFe_2O_4$ nanoparticles and ZFO/CN heterojunctions. The bare

g-C$_3$N$_4$ nanosheets show a strong absorption just at wavelength shorter than around 460 nm. Pure ZnFe$_2$O$_4$ nanoparticles show significant absorption both in the ultraviolet and visible regions. Upon the formation of heterojunctions, The ZFO/CN heterojunctions possess increased optical absorption especially in the visible region, and the absorption edge shows red-shift compared to the pure g-C$_3$N$_4$ nanosheets. Generally, the band gap energy (E_g) of semiconductor can be obtained by the Kubelka–Munk method [46]:

$$(\alpha h v)^n = A(h v - E_g) \qquad (1)$$

where α, h, v and A represent the absorption coefficient, Planck constant, light frequency and constant, respectively. The optical band gaps of g-C$_3$N$_4$ ($n = 0.5$ for indirect transition) and ZnFe$_2$O$_4$ ($n = 2$ for direct transition) were determined by a Tauc plot with a linear extrapolation, as shown in Fig. 4b. The E_g of g-C$_3$N$_4$ nanosheets and ZnFe$_2$O$_4$ nanoparticles are calculated to be 2.36 and 1.80 eV, respectively. Based on the E_g values, the valence band energy (E_{VB}) and conduction band energy (E_{CB}) of g-C$_3$N$_4$ nanosheets and ZnFe$_2$O$_4$ nanoparticles can be calculated by the following equations [47]:

$$E_{CB} = X - E_e - 0.5E_g \qquad (2)$$

$$E_{VB} = E_{CB} + E_g \qquad (3)$$

where X is the absolute electronegativity of semiconductor and E_e is the energy of free electrons on hydrogen scale (about 4.5 eV) [48]. The E_{CB} and E_{VB} of g-C$_3$N$_4$ nanosheets are calculated to be -0.95 and 1.41 eV, respectively. The E_{CB} and E_{VB} of ZnFe$_2$O$_4$ are -0.35 and 1.45 eV, respectively.

The separation and transfer ability of photogenerated electron–hole pairs is a crucial factor for photocatalysis. Photoluminescence (PL) spectra are applied to examine the photo-induced charge carrier excitation, migration, transfer and recombination processes of semiconductor photocatalysts. Figure 4c shows the PL spectra of g-C$_3$N$_4$ nanosheets and ZFO/CN heterojunctions. An obvious emission peak can be seen at approximately 460 nm, which is related to the band gap recombination of photogenerated carriers for g-C$_3$N$_4$ nanosheets. The lower PL intensity represents higher electron–hole separation efficiency, resulting in higher photocatalytic activity [49, 50]. Compared to the pure g-C$_3$N$_4$ nanosheets, ZFO/CN (except ZFO/CN-5) show lower PL intensity, revealing efficient suppression of the recombination between photogenerated electron–hole pairs. The PL spectrum of ZFO/CN-20 possesses the lowest intensity, indicating the excellent carriers separation and photocatalytic activity [51, 52]. The efficient interfacial charge migration and separation can be further investigated through the photoelectrochemical properties. Figure 4d shows the transient photocurrent (PC) response of g-C$_3$N$_4$ nanosheets and ZFO/CN-20. ZFO/CN-20 shows the highest photocurrent density. The larger photocurrent response reveals the higher electrons and holes separation efficiency. Therefore, the photoexcited carriers in ZFO/CN-20 are separated effectively and the photoexcited charge carriers have an improved lifetime during the photocatalytic degradation reaction. Electrochemical impedance spectroscopy (EIS) was performed to provide the evidence of the faster transportation of photoexcited electrons. Generally speaking, a higher mobility and separation of photoexcited electron–hole pairs would result in a smaller arc radius. As seen in Fig. 4e, g-C$_3$N$_4$ nanosheets display an arc radius value than ZFO/CN-20. The PC and EIS results indicate that the combination of ZnFe$_2$O$_4$ nanoparticles could greatly inhibit the recombination of electron–hole pairs in g-C$_3$N$_4$ nanosheets, and efficiently facilitate the separation of photogenerated charges at the interface between ZnFe$_2$O$_4$ nanoparticles and g-C$_3$N$_4$ nanosheets. These results were consistent with the PL analysis, which further validates that the introduction of ZnFe$_2$O$_4$ nanoparticles can enhance the photocatalytic performance.

Figure 4f reveals the M–H curves of g-C$_3$N$_4$ nanosheets, ZnFe$_2$O$_4$ nanoparticles and ZFO/CN-20 measured at room temperature. The corresponding zoomed M–H curves are displayed in Fig. S4. Obviously, the M–H curve of g-C$_3$N$_4$ nanosheets shows a linear shape, displaying nonmagnetic characteristic. The M–H curves of ZnFe$_2$O$_4$ and ZFO/CN-20 reveal S-like shape, and the coercivity (Hc) values are only about 13 and 15 Oe, respectively. These results suggest that ZnFe$_2$O$_4$ and ZFO/CN-20 show magnetic behavior at room temperature. The magnetization saturation (Ms) value of ZFO/CN-20 is 0.85 emu/g, smaller than that of ZnFe$_2$O$_4$ nanoparticles (14.2 emu/g). This is owing to the non-magnetic g-C$_3$N$_4$. Inset of Fig. 4f shows the photograph of magnetic separation tests of ZFO/CN-20. The transparent solution indicates that the magnetic ZFO/CN heterojunctions can be easily collected by an applied
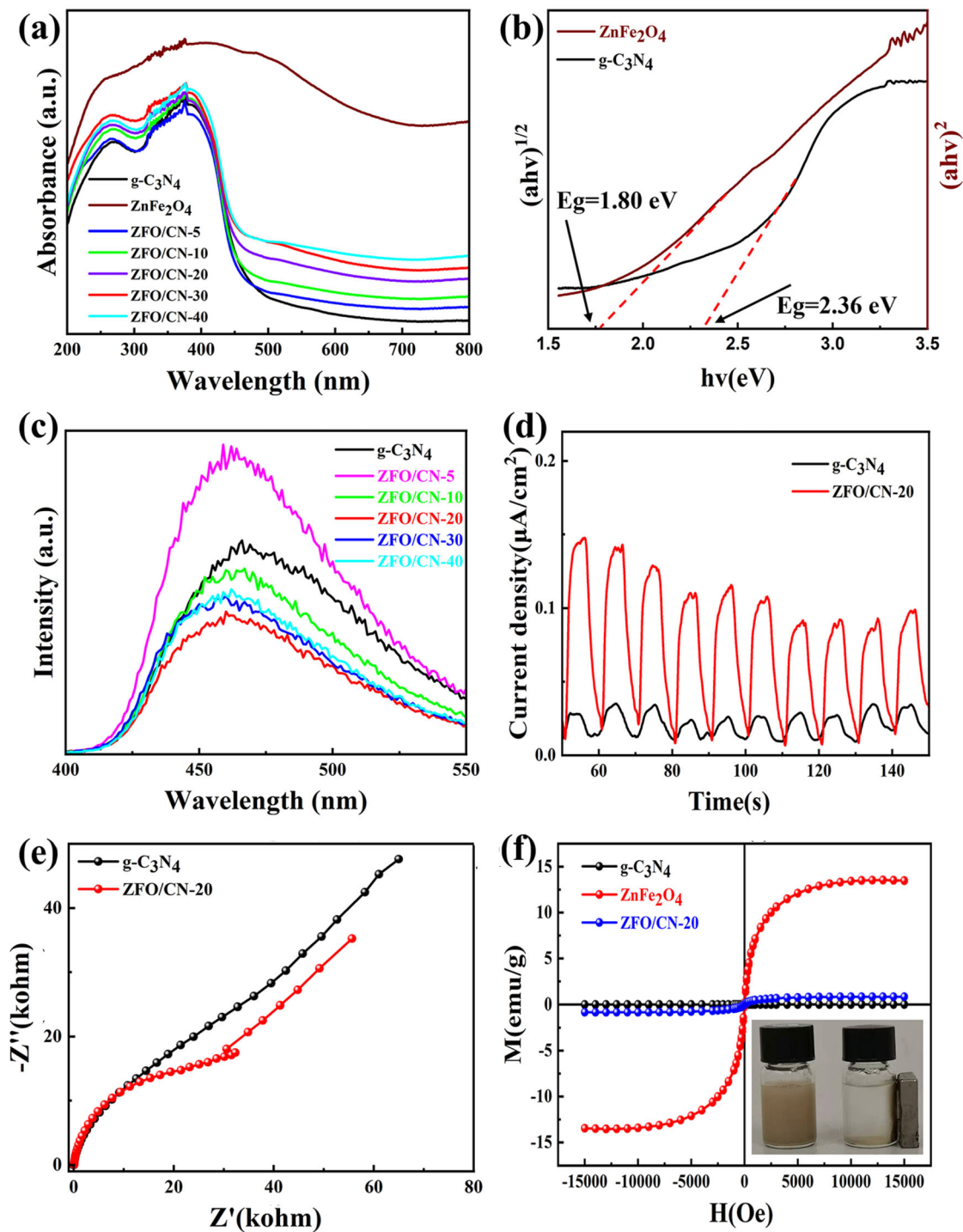
Fig. 4 a UV–vis absorption spectra of g-C$_3$N$_4$ nanosheets, ZnFe$_2$O$_4$ nanoparticles and ZFO/CN heterojunctions; **b** Kubelka–Munk plots of g-C$_3$N$_4$ nanosheets and ZnFe$_2$O$_4$ nanoparticles; **c** PL spectra of g-C$_3$N$_4$ nanosheets and ZFO/CN; **d** Transient photocurrent response and **e** EIS Nyquist spectra of g-C$_3$N$_4$ nanosheets and ZFO/CN-20; **f** M–H curves of g-C$_3$N$_4$ nanosheets, ZnFe$_2$O$_4$ nanosheets and ZFO/CN-20. Inset shows the photo of magnetic separation tests of ZFO/CN-20

magnet. These findings suggest that ZFO/CN heterojunctions have an excellent magnetic property, which brings convenience for recycling in wastewater management.

3.3 Photocatalytic performance

Methylene Blue (MB) is a typical cationic organic pollutant, which is widely found in various industrial and domestic wastewater. Besides, MB is generally used to evaluate the photocatalytic performance of semiconductor photocatalyst. Photocatalytic properties of the samples were evaluated by degradation of MB solution (20 ppm) under visible-light ($\lambda > 420$ nm) irradiation. Figure 5a shows the UV–vis absorption spectra of MB solution after photodegradation by ZFO/CN-20 at different time. The

absorption intensity of characteristic peak for MB (around 664 nm) decreased gradually by increasing the irradiation time, indicating that MB was gradually photodegraded. Figure 5b shows the comparison of photocatalytic activities curves for different photocatalysts. The ZFO/CN heterojunctions show greatly enhanced synergetic photocatalytic activities compared to the $ZnFe_2O_4$ and g-C_3N_4 monomers. The photocatalytic activities of ZFO/CN heterojunctions are sensitive to the content of $ZnFe_2O_4$ nanoparticles, which increase first and then decrease by increasing the amount of $ZnFe_2O_4$. Especially, ZFO/CN-20 shows the highest and fastest photocatalytic activity, in which 96.27% of MB was degraded in 3 h. The enhanced photocatalytic capacity of ZFO/CN heterojunctions is possibly due to that moderate amount of $ZnFe_2O_4$ nanoparticles could induce
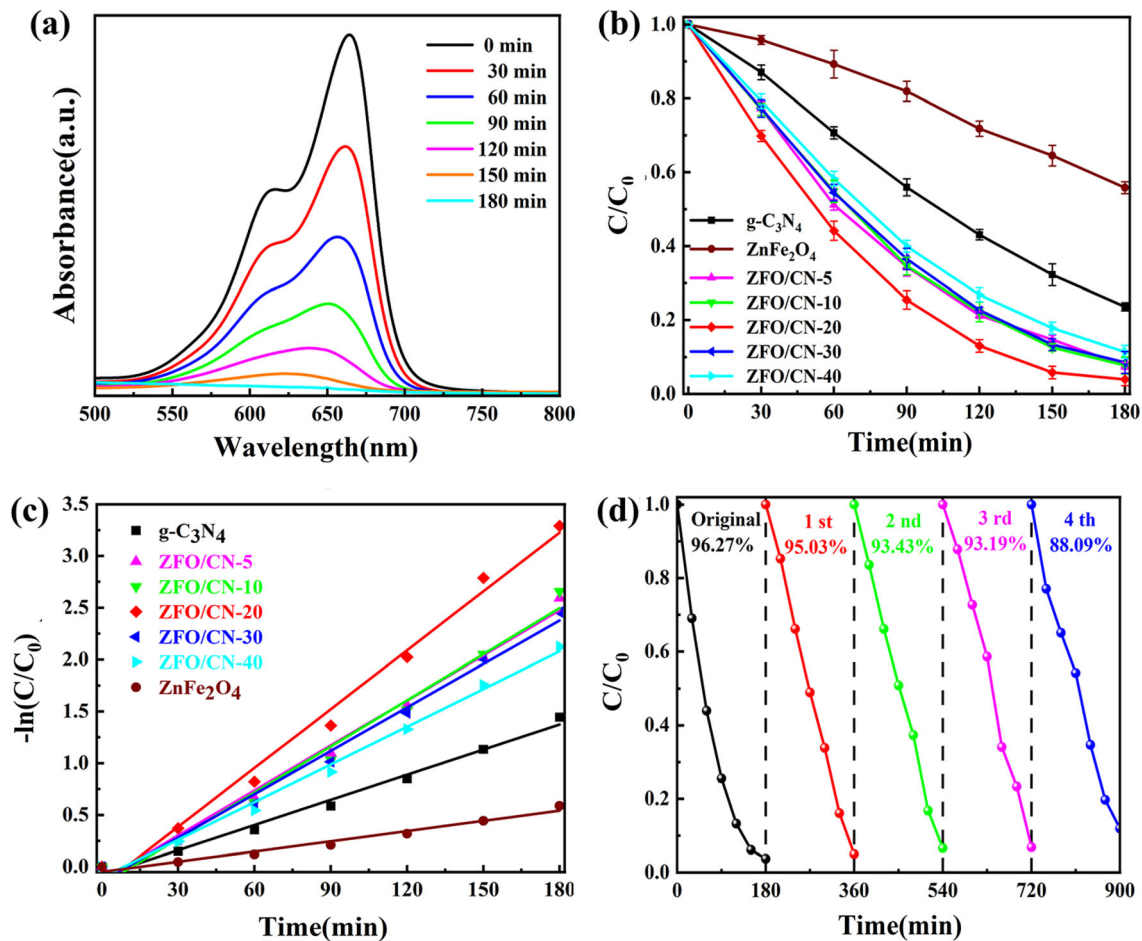

Fig. 5 Degradation of MB solution by g-C_3N_4 nanosheets, $ZnFe_2O_4$ nanoparticles and ZFO/CN heterojunctions: **a** UV–vis absorption spectra of MB solution by ZFO/CN-20 at different time; **b** Time profiles of the photocatalytic degradation of MB by different samples, error bars represent one standard deviation; **c** Pseudo-first-order kinetics fitted curves of different photocatalysts; **d** Recycling tests of ZFO/CN-20

abundant heterostructure interfaces and endow higher separation efficiency of photo-induced electron–hole pairs. Continuously increasing the amount of $ZnFe_2O_4$ nanoparticles may result in the aggregation of $ZnFe_2O_4$ on the surface of g-C_3N_4 nanosheets, reducing the amount of active sites and heterostructure interfaces.

Pseudo-first-order kinetics model was used to estimate the reaction kinetics of photocatalysts [46]:

$$-\ln(C_t/C_0) = kt \tag{4}$$

where C_0 is the initial concentration, C_t is the remaining concentration at different irradiation time, t is the irradiation time, and k (min^{-1}) is the apparent first-order rate constant. Figure 5c shows the pseudo-first-order kinetics fitted curves of different photocatalysts. Compared to g-C_3N_4 and $ZnFe_2O_4$ monomers, the ZFO/CN heterojunctions show enhanced degradation rates due to the synergistic effect, which increases first and then decreases by increasing the content of $ZnFe_2O_4$ nanoparticles. Among them, ZFO/CN-20 exhibits the highest degradation rate of 0.019 min^{-1}, which is nearly 2.4 and 6.3 times higher than that of g-C_3N_4 (0.008 min^{-1}) and $ZnFe_2O_4$ (0.003 min^{-1}), respectively. These results suggest that ZFO/CN-20 shows significantly enhanced photocatalytic performance for MB degradation, which is attributed to the unique heterojunction structure.

The reusability is another crucial factor for the practical applications of catalysts. Recycling experiments of optimal ZFO/CN-20 is shown in Fig. 5d. The degradation rate of ZFO/CN-20 has no apparent deactivation after four repeated cycles, suggesting good chemical stability and reusability. 88.09% of MB was still degraded after four cycles. The slight decline after cycles is probably due to the photocatalyst loss during the collection. To further confirm the stability, the ZFO/CN-20 heterojunctions after four cycles were characterized by XRD, SEM and XPS techniques, as shown in Fig. S5. After four cycling, XRD patterns (Fig. S5a) of ZFO/CN-20 remains the phase without discrepancy, implying that ZFO/CN-20 shows great structure stability during the photocatalytic process. Besides, the XPS spectra (Fig. S5c-h) confirm that the chemical composition and electric states of all the elements in ZFO/CN-20 are similar to the fresh samples, further suggests the stability. The SEM image (Fig. S5b) suggests that the morphology of the recycled photocatalyst is a little different from the fresh ZFO/CN-20 (Fig. S2d). This is mainly due to

that photo-induced electron–hole migration may slightly damage the microstructure of photocatalyst during the multiple photocatalytic recycling, which can reasonably explain the slightly loss of 8.2% for ZFO/CN-20 photocatalyst after four cycles. The characterizations of recycled photocatalyst (Fig. S5) suggest that the recycling can gently change the morphology, but has little influence on the phase, chemical composition and electric states of ZFO/CN heterojunction.

The universal suitability of ZFO/CN heterojunctions was further studied by photodegradation of rhodamine B (RhB, another typical cationic organic pollutant) and methyl orange (MO, a typical anionic organic pollutant), as shown in Fig. S6. Compared to the g-C_3N_4 monomer, ZFO/CN-20 shows improved photocatalytic efficiency. The photodegradation efficiencies of RhB and MO by ZFO/CN-20 are 92.4 and 73.17%, respectively, much higher than those values by g-C_3N_4 monomer (81.22% for RhB and 25.76% for MO), as shown in Fig. S6a-d. The kinetic constants of ZFO/CN-20 for degradation of RhB and MO are 0.015 and 0.007 min^{-1}, respectively, which are about 1.7 and 3.5 times higher than the g-C_3N_4 monomer (0.009 min^{-1} for RhB, 0.002 min^{-1} for MO), as displayed in Fig. S6e and f. Table S3 compares the photocatalytic performance between $ZnFe_2O_4$/g-C_3N_4 and other g-C_3N_4 based materials. Obviously, the $ZnFe_2O_4$/g-C_3N_4 heterostructures show excellent photocatalytic performance at a relatively short time and large pollutant concentration. These results suggest that ZFO/CN heterojunctions show high-efficient photocatalytic degradation performance to different kinds of organic pollutants.

3.4 Mechanism analysis

The light-harvesting capacity, photoelectrochemical properties and PL properties of g-C_3N_4, $ZnFe_2O_4$, and $ZnFe_2O_4$/g-C_3N_4 were studied to deeply understand the photocatalytic mechanism of ZFO/CN. The photo-induced reactive species, including photogenerated holes (h^+), e^-, hydroxyl radicals (·OH) and superoxide radicals (·O_2^-) are involved in the photocatalytic degradation process. It is necessary to study the roles through the trapping experiment of the photo-induced reactive species. Four trapping agents, including EDTA-2Na, $AgNO_3$, BQ and IPA were employed as the scavengers of h^+, e^-, ·O_2^- and ·OH, respectively [23, 37]. The reactive species capture

experiments were carried out by g-C_3N_4 and ZFO/CN-20. During all the trapping experiments, the amount of trapping agents was kept to be 1 mM. As shown in Fig. 6a and b, the photocatalytic efficiencies of MB by ZFO/CN-20 were decreased from original 96.27% (without trapping agent) to 82.25% (with IPA), 85.61% (with BQ) and 55.76% (with AgNO$_3$), respectively. For g-C_3N_4 monomer (Fig. S7), the photocatalytic efficiencies of MB were also reduced from original 76.42% (without trapping agent) to 71.29% (with IPA), 45.65% (with BQ) and 49.04% (with AgNO$_3$), respectively. The capture experiments show that the ·OH, ·O$_2^-$ and e^- species improve the photocatalytic activity for MB degradation. Among them, photogenerated electrons (e^-) play a crucial role in the photocatalytic system of g-C_3N_4-based materials, while ·OH and ·O$_2^-$ are involved in the

photocatalytic process. The addition of EDTA-2Na can greatly improve the photocatalytic efficiency of g-C_3N_4 monomer, in which the photocatalytic efficiency is boosted from 76.42 to 98.98% (Fig. S7). According to the mechanism of semiconductor photocatalytic reaction, e^- can reduce O$_2$ to ·O$_2^-$ by a reduction reaction, but there is a serious recombination phenomenon between e^- and h^+ [53]. EDTA-2Na, as the scavenger of h^+, plays a role in improving the separation efficiency of photogenerated electron–hole pairs. When EDTA-2Na was added, the main reason for the excessive increase of photocatalytic efficiencies is due to the improved separation efficiency (e^- and h^+), resulting in the increased quantity of ·O$_2^-$ involved in the degradation of MB. For ZFO/CN-20 (Fig. 6a), the degradation efficiencies of MB reach 96.21% in 90 min and 96.99% in 180 min after
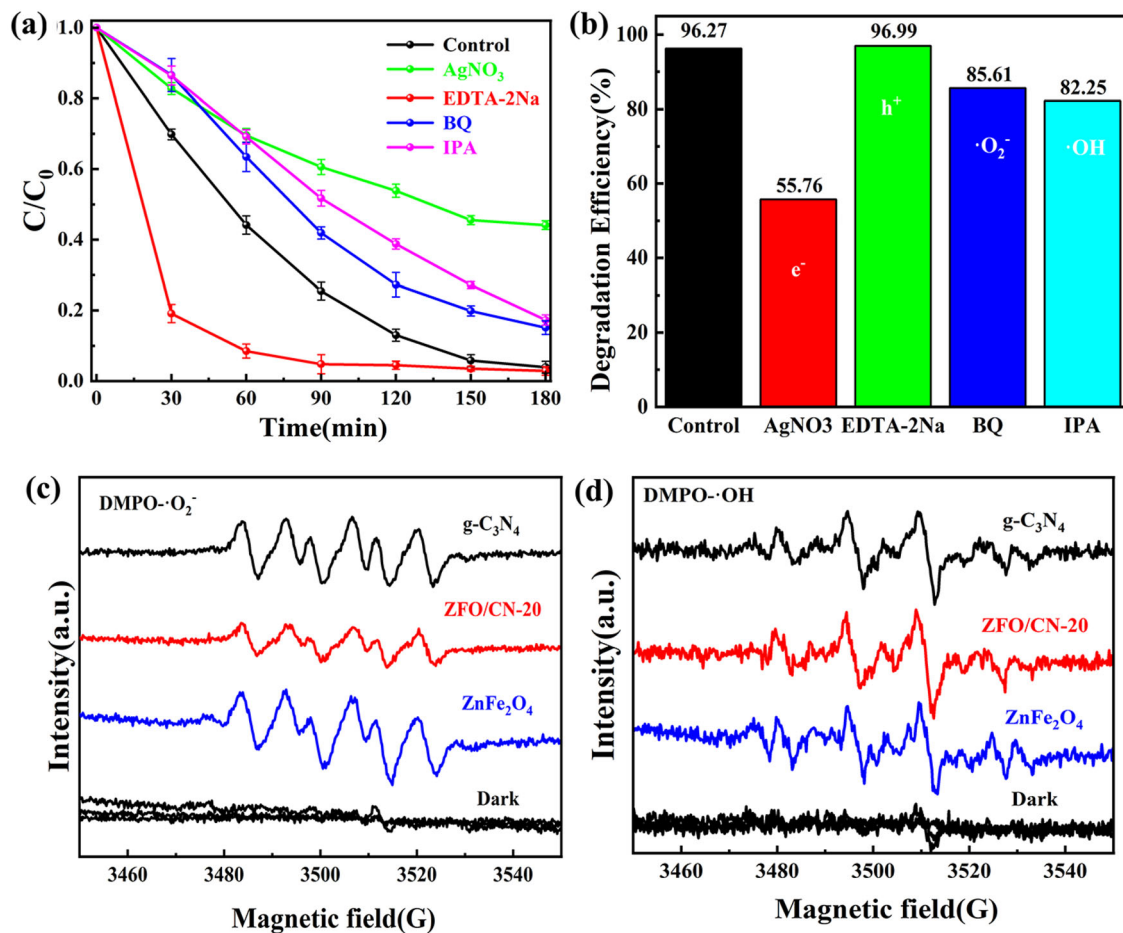

Fig. 6 **a**, **b** Capture experiments of photodegradation of MB solution by ZFO/CN-20 after adding different trapping agents, error bars represent one standard deviation; ESR spectra of *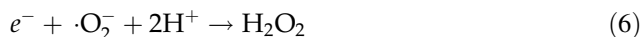*c** DMPO-·O$_2^-$ and **d** DMPO-·OH for g-C_3N_4 nanosheets, ZnFe$_2$O$_4$ nanoparticles and ZFO/CN-20 under dark condition and visible light irradiation

introducing EDTA-2Na, while the degradation efficiencies are 74.46% in 90 min and 96.27% in 180 min without EDTA-2Na. The introducing EDTA-2Na has little influence on the final photocatalytic efficiency, but greatly boosts the photocatalytic rate. This suggests that $ZnFe_2O_4$ nanoparticles can improve the separation efficiency of photogenerated electron–hole pairs in ZFO/CN heterojunctions and avoid the rapid recombination in $g-C_3N_4$ monomer. The capture experiment results of $g-C_3N_4$ and ZFO/CN-20 indicated that ZFO/CN heterojunction behaves higher separation efficiency of photogenerated electron–hole pairs and faster photocatalytic rate than $g-C_3N_4$ monomer.

To determine if $\cdot OH$ and $\cdot O_2^-$ radicals are generated during the photocatalytic process, ESR technique is carried out under dark condition and visible light irradiation for comparison, as shown in Fig. 6c and d. During the detection, 5,5-Dimethyl-l-pyrroline N-oxide (DMPO) was used to trap $\cdot OH$ in aqueous solution and $\cdot O_2^-$ in methanol solution, which can produce the adducts of DMPO-$\cdot OH$ and DMPO-$\cdot O_2^-$, respectively [39]. Under the darkness environment, no ESR signals are detected in the DMPO-containing aqueous solution or methanol solution with $g-C_3N_4$ nanosheets, $ZnFe_2O_4$ nanoparticles and ZFO/CN-20. When the solutions were irradiated by visible light, the characteristic peaks of DMPO-$\cdot O_2^-$ adduct (Fig. 6c) and DMPO-$\cdot OH$ adduct (Fig. 6d) can be detected in the solutions with $g-C_3N_4$ nanosheets, $ZnFe_2O_4$ nanoparticles and ZFO/CN-20. These results demonstrate that active species of $\cdot O_2^-$ and $\cdot OH$ radicals are definitely generated by photogenerated electrons under visible light irradiation.

As described in Fig. 6, the active species trapping experiment and ESR analysis demonstrates that $\cdot O_2^-$ and $\cdot OH$ radicals are produced in the photocatalytic reaction system. However, the calculated CB potentials of $g-C_3N_4$ (− 0.95 eV *vs*. Normal Hydrogen Electrode (NHE)) and $ZnFe_2O_4$ (− 0.35 eV *vs*. NHE) are more negative than the standard redox potentials of $O_2/\cdot O_2^-$ (− 0.33 eV *vs*. NHE). Besides, the standard redox potentials of $H_2O/\cdot OH$ (2.72 eV *vs*. NHE) and $OH^-/\cdot OH$ (1.99 eV *vs*. NHE) are more positive than the VB potentials of $g-C_3N_4$ (1.41 eV *vs*. NHE) and $ZnFe_2O_4$ (1.45 eV *vs*. NHE). This implies that the photoexcited holes in the VB of $g-C_3N_4$ and $ZnFe_2O_4$ cannot directly oxidize the adsorbed H_2O molecules or surface hydroxyl group to form $\cdot OH$ [54, 55].

Therefore, an indirect way for the formation of $\cdot O_2^-$ and $\cdot OH$ radicals is proposed. The photogenerated electrons on the CB of $g-C_3N_4$ and $ZnFe_2O_4$ react with the resolved O_2, forming $\cdot O_2^-$ radical species. Then the photogenerated electrons would react with $\cdot O_2^-$ and H^+ to produce H_2O_2, which could be further reduced to $\cdot OH$ radicals. The process is speculated as follows [56, 57]:

$$O_2 + e^- \rightarrow \cdot O_2^- \qquad (5)$$

$$e^- + \cdot O_2^- + 2H^+ \rightarrow H_2O_2 \qquad (6)$$

$$e^- + H_2O_2 \rightarrow \cdot OH + OH^- \qquad (7)$$

As described above, if the active species of $\cdot O_2^-$ and $\cdot OH$ radicals are generated according to the Eqs. (5–7), H_2O_2 should be also spontaneously produced during the photocatalytic process. In order to verify this hypothesis, we further carried out the H_2O_2 detection experiments under UV–vis illumination. Figure S8a shows the UV–vis absorption spectra of aqueous solution with different contents of H_2O_2. Obviously, the absorption intensity of characteristic peak for H_2O_2 (around 350 nm) increases by increasing the H_2O_2 content. Figure 7a displays the fitted curve of the relationship between H_2O_2 contents and absorbency in UV–vis region, which is obtained from Fig. S8a. The H_2O_2 contents and absorbency shows typical linear relationship. Figure S8b-d reveals the UV–vis absorption spectra of aqueous solution containing $g-C_3N_4$, $ZnFe_2O_4$ and ZFO/CN-20 photocatalysts, which were irradiated at different time. Under ultra-voilet illumination, the characteristic absorption peak for H_2O_2 can be obviously observed in the aqueous solutions containing $g-C_3N_4$, $ZnFe_2O_4$ and ZFO/CN-20 photocatalysts. Besides, the absorption intensity of characteristic peak for H_2O_2 increased gradually as the irradiation time increases. These phenomena demonstrate that a certain amount of H_2O_2 is spontaneously generated during the photocatalytic process, verifying the about hypothesis. Figure 7b shows the concentration of spontaneously produced H_2O_2 species by $g-C_3N_4$, $ZnFe_2O_4$ and ZFO/CN-20 at different illumination time, which is simulated according Figs. 7a and S8. Obviously, the $g-C_3N_4$ monomer shows the highest yield of H_2O_2 (327.8 μM). However, the photocatalytic performance is lower than ZFO/CN-20, as described before. This is mainly due to the high electron–hole recombination rate in $g-C_3N_4$
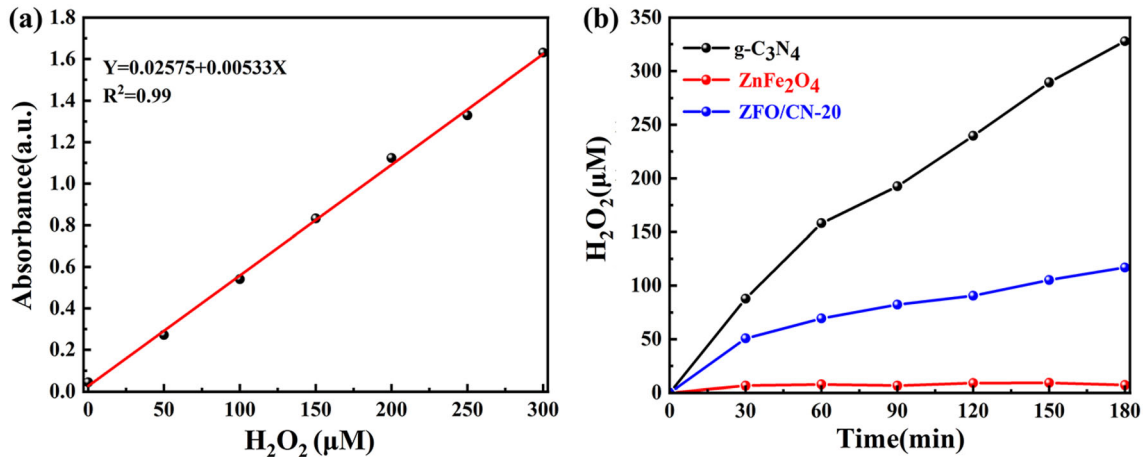
Fig. 7 **a** Fitted curve of the relationship between H_2O_2 contents and absorbency in UV–vis region; **b** The concentration of spontaneously produced H_2O_2 species by g-C_3N_4, $ZnFe_2O_4$ and ZFO/CN-20 at different illumination time

nanosheets. The photogenerated electrons in g-C_3N_4 nanosheets rapidly recombine with the holes, and cannot adequately react with H_2O_2, resulting in the accumulation of H_2O_2. Meanwhile, ·OH radicals were slowly generated by g-C_3N_4 monomer upon photoexcitation and the increasing concentration of H_2O_2 leads to the production of a new radical (·OOH), which shows a considerably lower oxidation potential than that of ·OH radicals [31, 58]. On the contrary, although ZFO/CN-20 shows a lower yield of H_2O_2 (116.9 μM), but the separation of photogenerated electron–hole pairs is effectively promoted. The spontaneously produced H_2O_2 species can adequately react with the photogenerated electrons, resulting in abundant active species of $·O_2^-$ and ·OH radicals for photocatalysis. The H_2O_2 yield of $ZnFe_2O_4$ monomer is only 7.2 μM, which can be negligible (Fig. 7b). g-C_3N_4 and $ZnFe_2O_4$ can continuously supply H_2O_2 and iron ions, respectively. Self-Fenton reaction wouldn't happen in the $ZnFe_2O_4$ monomer.

Based on the above investigations, the photocatalytic mechanism of ZFO/CN heterojunctions is proposed, as depicted in Fig. 8. Under visible-light irradiation, the g-C_3N_4 and $ZnFe_2O_4$ components generate electron–hole pairs. The photogenerated electrons generated from VB migrate to CB, leaving holes in the VB. According to the results of XPS characterization, we consider that the photogenerated electrons produced in g-C_3N_4 nanosheets transferred to the CB of $ZnFe_2O_4$ nanoparticles, and the holes produced in the $ZnFe_2O_4$ migrated from $ZnFe_2O_4$ to g-C_3N_4. This is due to the lower valence
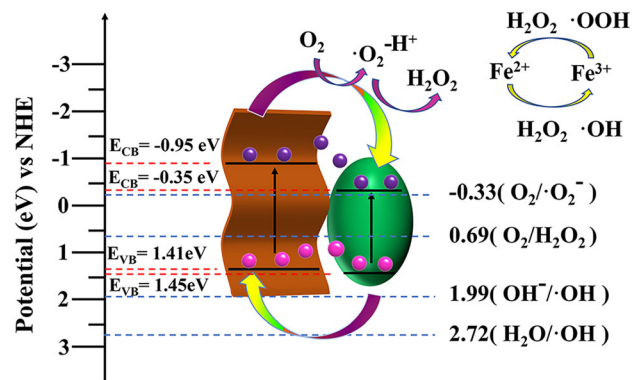

Fig. 8 Band structure and photocatalytic mechanism of the ZFO/CN heterostructures

band potential and more negative conduction band potential of g-C_3N_4. The photo-induced charge pairs effectively migrate from the opposite direction, promoting the separation efficiency and enhancing the photocatalytic activity. The responsibilities of the photogenerated electrons (e^-) mainly have the following aspects: (1) e^- was favored for the generation of active species (·OH and $·O_2^-$) and H_2O_2 (Eqs. (5–7)); (2) The self-redox reaction process of Fe ions was realized by using the reducibility of e^-, accelerating the regeneration from Fe^{3+} to Fe^{2+}. On one hand, some transferred electrons in the CB combine with adsorbed O_2, yielding $·O_2^-$ radicals for photocatalytic reaction. On the other hand, some electrons react with O_2 and resolved H^+ to produce H_2O_2, which will be further reduced into ·OH radicals. The iron-based nanomaterials show photo-Fenton reaction, due to that the ferric ions in the crystal lattice can

absorb the chemical oxidants (H_2O_2) and create highly reactive ·OH radicals for photocatalytic reaction. However, in photo-self-Fenton system, the degradation efficiency is usually higher than the Fenton reaction and photo-Fenton reaction because of the fast conversion of Fe^{3+} into Fe^{2+} ions, high utilization and activation efficiency of self-production H_2O_2 [30, 42]. A self-redox reaction process of the Fe ions induces the H_2O_2 to give ·OH radicals. Fe^{3+} can not only participate in the photo-self-Fenton reaction, but also promote the separation of photogenerated electron–hole pairs via gains electrons. Finally, the pollutants are gradually decomposed by $·O_2^-$ and ·OH into degraded products.

4 Conclusions

In summary, magnetic $ZnFe_2O_4$/g-C_3N_4 heterojunctions were constructed as visible-light-driven photocatalyst. In the heterojunctions, tiny $ZnFe_2O_4$ nanoparticles were anchored on the g-C_3N_4 nanosheets, which can sufficiently contact with each other, inducing a higher specific surface area and plentiful active sites for photocatalysis. The specific structure and synergistic effect make $ZnFe_2O_4$/g-C_3N_4 heterojunctions behave improved photocatalytic properties in comparison with the onefold g-C_3N_4 nanosheets or $ZnFe_2O_4$ nanoparticles, which can efficiently photodegradate three different pigments of methylene blue, methyl orange and rhodamine B. The loading tiny $ZnFe_2O_4$ nanoparticles can greatly enhance the visible-light absorption capacity and accelerate the photo-induced electron–hole separation of g-C_3N_4 nanosheets, leading to boosted photocatalytic performance. Photocatalytic mechanism studies show that photogenerated electrons play a crucial role in the photocatalytic system. Besides, the $ZnFe_2O_4$/g-C_3N_4 heterojunctions are a photo-self-Fenton system, which can spontaneously produce H_2O_2 under illumination, forming active species of $·O_2^-$ and ·OH radicals. The synergistic effect of ·OH and $·O_2^-$ radicals is responsible for degradation organic pollutants. In addition, the $ZnFe_2O_4$/g-C_3N_4 heterojunction photocatalysts show excellent stability after cycling, and can be easily separated by an applied magnet, which is important for practical applications.

Author contributions

XL: date curation, investigation and paper writing. HX and XY: characterization. DW, YZ: investigation. JF: methodology, resources. XZ, XL: methodology, reviewing, editing. XZ: supervision and methodology.

Data availability

Data will be made available upon reasonable academic request within the limitations of informed consent by the corresponding author upon acceptance.

Declarations

Conflict of interest   The authors reported no conflict of interest.

Ethical approval   The authors claim that this work described has not been published previously, that it is not under consideration for publication elsewhere, that its publication is approved by all authors and tacitly or explicitly by the responsible authorities where the work was carried out.

Supplementary Information: The online version contains supplementary material available at https://doi.org/10.1007/s10854-023-10640-2.

References

1. Q. Wang, Z.M. Yang, Industrial water pollution, water environment treatment, and health risks in China. Environ. Pollut.

218, 358–365 (2016). https://doi.org/10.1016/j.envpol.2016.07.011

2. Y.S. Zhou, G. Chen, Y.G. Yu, L.C. Zhao, J.X. Sun, F. He, H.J. Dong, A new oxynitride-based solid state z-scheme photocatalytic system for efficient Cr (VI) reduction and water oxidation. Appl. Catal. B **183**, 176–184 (2016). https://doi.org/10.1016/j.apcatb.2015.10.040

3. A. Alsbaiee, B.J. Smith, L.L. Xiao, Y.H. Ling, D.E. Helbling, W.R. Dichtel, Rapid removal of organic micropollutants from water by a porous beta-cyclodextrin polymer. Nature **529**, 190–194 (2016). https://doi.org/10.1038/nature16185

4. S.D. Richardson, T.A. Ternes, Water analysis: emerging contaminants an-d current issues. Anal. Chem. **86**, 2813–2848 (2014). https://doi.org/10.1021/ac500508t

5. B. Jain, A.K. Singh, H. Kim, E. Lichtfouse, V.K. Sharma, Treatment of organic pollutants by homogeneous and heterogeneous Fenton reaction pro-cesses. Environ. Chem. Lett. **16**, 947–967 (2018). https://doi.org/10.1007/s10311-018-0738-3

6. G. Zhao, W.C. Li, H.Y. Zhang, W. Wang, Y.P. Ren, Single atom Fe-dispersed graphitic carbon nitride (g-C_3N_4) as a highly efficient peroxymonosulfate photocatalytic activator for sulfamethoxazole degradation. Chem. Eng. J. **430**, 132937 (2022). https://doi.org/10.1016/j.cej.2021.132937

7. Y.P. Zhu, R.L. Zhu, L.X. Yan, H.Y. Fu, Y.F. Xi, H.J. Zhou, G.Q. Zhu, J.X. Zhu, H.P. He, Visible-light Ag/AgBr/ferrihydrite catalyst with enhanced heterogeneous photo-Fenton reactivity via electron transfer from Ag/AgBr to ferrihydrite. Appl. Catal. B **239**, 280–289 (2018). https://doi.org/10.1016/j.apcatb.2018.08.025

8. L.J. Xu, J.L. Wang, Fenton-like degradation of 2,4-dichlorophenol using Fe_3O_4 magnetic nanoparticles. Appl. Catal. B **123–124**, 117–126 (2012). https://doi.org/10.1016/j.apcatb.2012.04.028

9. Y.B. Ding, X.R. Wang, L.B. Fu, X.Q. Peng, C. Pan, Q.H. Mao, C.J. Wang, J.C. Yan, Nonradicals induced degradation of organic pollutants by peroxydisulfate (PDS) and peroxymonosulfate (PMS): recent advances a-nd perspective. Sci. Total Environ. **765**, 142794 (2021). https://doi.org/10.1016/j.scitotenv.2020.142794

10. X.D. Zhang, J. Wang, B.B. Xiao, Y.J. Pu, Y.C. Yang, J.S. Geng, D.Y. Wang, X.J. Chen, Y.X. Wei, K. Xiong, Y.F. Zhu, Resin-based pho-to-self-Fenton system with intensive mineralization by the synergistic effect of holes and hydroxyl radicals. Appl. Catal. B **315**, 121525 (2022). https://doi.org/10.1016/j.apcatb.2022.121525

11. D.L. Yuan, C. Zhang, S.F. Tang, X. Li, J.C. Tang, Y.D. Rao, Z.B. Wang, Q.R. Zhang, Enhancing CaO_2 fenton-like process by Fe(II)-oxalic acid complexation for organic wastewater treatment. Water Res. **163**, 114861 (2019). https://doi.org/10.1016/j.watres.2019.114861

12. J. Li, Y.J. Wan, Y.J. Li, G. Yao, B. Lai, Surface Fe(III)/Fe(II) cycle pr-omoted the degradation of atrazine by peroxymonosulfate activation in the presence of hydroxylamine. Appl. Catal. B **256**, 117782 (2019). https://doi.org/10.1016/j.apcatb.2019.117782

13. Y.X. Qin, G.Y. Li, Y.P. Gao, L.Z. Zhang, Y.S. Ok, T. An, Persistent free radicals in carbon-based materials on transformation of refractory organic contaminants (ROCs) in water: a critical review. Water Res. **137**, 130–143 (2018). https://doi.org/10.1016/j.watres.2018.03.012

14. H.Y. Zhou, J.L. Peng, J.Y. Li, J.J. You, L.D. Lai, R. Liu, Z. Ao, G. Yao, B. Lai, Metal-free black-red phosphorus as an efficient heterogeneous reductant to boost Fe^{3+}/Fe^{2+} cycle for peroxymonosulfate activation. Water Res. **188**, 116529 (2021). https://doi.org/10.1016/j.watres.2020.116529

15. S.O. Ganiyu, M.H. Zhou, C.A. Martínez-Huitle, Heterogeneous electro-Fenton and photoelectro-Fenton processes: a critical review of fundamental principles and application for water/wastewater treatment. Appl. Catal. B **235**, 103–129 (2018). https://doi.org/10.1016/j.apcatb.2018.04.044

16. D.Q. Tian, H.Y. Zhou, H. Zhang, P. Zhou, J.J. You, G. Yao, Z.C. Pan, Y. Liu, B. Lai, Heterogeneous photocatalyst-driven persulfate activation process under visible light irradiation: from basic catalyst design principles to novel enhancement strategies. Chem. Eng. J. **428**, 131166 (2022). https://doi.org/10.1016/j.cej.2021.131166

17. X.C. Wang, K. Maeda, A. Thomas, K. Takanabe, G. Xin, J.M. Carlsson, K. Domen, M. Antonietti, A metal-free polymeric photocatalyst for hydrogen production from water under visible light. Nat. Mater. **8**, 271–275 (2009). https://doi.org/10.1038/nmat2317

18. B.C. Zhu, P.F. Xia, Y. Li, W.K. Ho, J.G. Yu, Fabrication and photoc-atalytic activity enhanced mechanism of direct z-scheme g-C_3N_4/Ag_2WO_4 p-hotocatalyst. Appl. Surf. Sci. **391**, 175–183 (2017). https://doi.org/10.1016/j.apsusc.2016.07.104

19. V. Hasija, V.H. Nguyen, A. Kumar, P. Raizada, V. Krishnan, A.A.P. Khan, P. Singh, E. Lichtfouse, C.Y. Wang, P.T. Huong, Advanced activation of persulfate by polymeric g-C_3N_4 based photocatalysts for environmental remediation: a review. J. Hazard. Mater. **413**, 125324 (2021). https://doi.org/10.1016/j.jhazmat.2021.125324

20. Z.W. Zhao, Y.J. Sun, F. Dong, Graphitic carbon nitride based nanocomposites: a review. Nanoscale **7**, 15–37 (2015). https://doi.org/10.1039/c4nr03008g

21. X.X. Yang, Y.L. Ye, J.D. Sun, Z.J. Li, J.F. Ping, X.L. Sun, Recent Advances in g-C_3N_4-Based Photocatalysts for Pollutant degradation and bacterial disinfection: design strategies,

mechanisms, and applications. Small **18**, 2105089 (2022). https://doi.org/10.1002/smll.202105089

22. S. Kumar, B. Kumar, A. Baruah, V. Shanker, Synthesis of magnetically separable and recyclable g-C$_3$N$_4$-Fe$_3$O$_4$ hybrid nanocomposites with enhanced photocatalytic performance under visible-light irradiation. J. Phys. Chem. C **117**, 26135–26143 (2013). https://doi.org/10.1021/jp409651g

23. B. Palanivel, S.D.M. Perumal, T. Maiyalagan, V. Jayarman, C. Ayyappan, M. Alagiri, Rational design of ZnFe$_2$O$_4$/g-C$_3$N$_4$ nanocomposite for enhanced photo-Fenton reaction and supercapacitor performance. Appl. Surf. Sci. **498**, 143807 (2019). https://doi.org/10.1016/j.apsusc.2019.143807

24. P.L. Liang, L.Y. Yuan, H. Deng, X.C. Wang, L. Wang, Z.J. Li, S.Z. Luo, W.Q. Shi, Photocatalytic reduction of uranium(VI) by magnetic ZnFe$_2$O$_4$ under visible light. Appl. Catal. B **267**, 118688 (2020). https://doi.org/10.1016/j.apcatb.2020.118688

25. Y. Jiang, L.D. Sun, N. Li, L. Gao, K. Chattopadhyay, Metal-doped ZnFe$_2$O$_4$ nanoparticles derived from Fe-bearing slag with enhanced visible-light photoactivity. Ceram. Int. **46**, 28828–28834 (2020). https://doi.org/10.1016/j.ceramint.2020.08.048

26. K.V. Savunthari, S. Shanmugam, Effect of co-doping of bismuth, copper and cerium in zinc ferrite on the photocatalytic degradation of bisphenol A. J. Taiwan Inst. Chem. Eng. **101**, 105–118 (2019). https://doi.org/10.1016/j.jtice.2019.04.042

27. Q. Gao, Z. Wang, J.X. Li, B. Liu, C.G. Liu, Rational design of direct z-scheme magnetic ZnIn$_2$S$_4$/ZnFe$_2$O$_4$ heterojunction toward enhanced photocatalytic wastewater remediation. Environ. Sci. Pollut. Res. **30**, 16438–16448 (2023). https://doi.org/10.1007/s11356-022-23236-w

28. V.S. Kirankumar, S. Sumathi, A review on photodegradation of organic pollutants using spinel oxide. Mater. Today Chem. **18**, 100355 (2020). https://doi.org/10.1016/j.mtchem.2020.100355

29. E. Prabakaran, T. Velempini, M. Molefe, K. Pillay, Comparative study of KF, KCl and KBr doped with graphitic carbon nitride for superior photocatalytic degradation of methylene blue under visible light. J. Mater. Res. Technol. **15**, 6340–6355 (2021). https://doi.org/10.1016/j.jmrt.2021.10.128

30. J. Liu, G. Liu, C.Y. Yuan, L. Chen, X.Y. Tian, M. Fang, Fe$_3$O$_4$/ZnFe$_2$O$_4$ micro/nanostructures and their heterogeneous efficient Fenton-like visible-light photocatalysis process. New J. Chem. **42**, 3736–3747 (2018). https://doi.org/10.1039/c7nj04548d

31. S. Borthakur, L. Saikia, ZnFe$_2$O$_4$@g-C$_3$N$_4$ nanocomposites: An efficient cat-alyst for Fenton-like photodegradation of environmentally pollutant Rhodami-ne B. J. Environ. Chem. Eng. **7**, 103035 (2019). https://doi.org/10.1016/j.jece.2019.103035

32. B. Palanivel, V. Jayaraman, C. Ayyappan, M. Alagiri, Magnetic binary metal oxide intercalated g-C$_3$N$_4$: energy band tuned p-n heterojunction towards Z-scheme photo-Fenton phenol reduction and mixed dye degradation. J. Water Process. Eng. **32**, 100968 (2019). https://doi.org/10.1016/j.jwpe.2019.100968

33. T. Xiong, H. Wang, Y. Zhou, Y.J. Sun, W.L. Cen, H.W. Huang, Y.X. Zhang, F. Dong, KCl-mediated dual electronic channels in layered g-C$_3$N$_4$ for enhanced visible light photocatalytic NO removal. Nanoscale **10**, 8066–8074 (2018). https://doi.org/10.1039/c8nr01433g

34. X.Y. Lu, J. Xie, X.B. Chen, X. Li, Engineering MPx (M = Fe, Co or Ni) interface electron transfer channels for boosting photocatalytic H$_2$ evolution over g-C$_3$N$_4$/MoS$_2$ layered heterojunctions. Appl. Catal. B **252**, 250–259 (2019). https://doi.org/10.1016/j.apcatb.2019.04.012

35. P.F. Xia, B.C. Zhu, B. Cheng, J.G. Yu, J.S. Xu, 2D/2D g-C$_3$N$_4$/MnO$_2$ nanocomposite as a direct z-scheme photocatalyst for enhanced photocataly-tic activity. ACS Sustain. Chem. Eng. **6**, 965–973 (2017). https://doi.org/10.1021/acssuschemeng.7b03289

36. M. Wu, J. Zhang, B.B. He, H.W. Wang, R. Wang, Y.S. Gong, In-situ construction of coral-like porous P-doped g-C$_3$N$_4$ tubes with hybrid 1D/2D architecture and high efficient photocatalytic hydrogen evolution. Appl. Catal. B **241**, 159–166 (2019). https://doi.org/10.1016/j.apcatb.2018.09.037

37. H. Tang, R. Wang, C.X. Zhao, Z.P. Chen, X.F. Yang, D. Bukhvalov, Z.X. Lin, Q.Q. Liu, Oxamide-modified g-C$_3$N$_4$ nanostructures: tailoring surface topography for high-performance visible light photocatalysis. Chem. Eng. J. **374**, 1064–1075 (2019). https://doi.org/10.1016/j.cej.2019.06.029

38. S.W. Zhang, J.X. Li, M.Y. Zeng, G.X. Zhao, J.Z. Xu, W.P. Hu, X.K. Wang, In situ synthesis of water-soluble magnetic graphitic carbon nitride photocatalyst and its synergistic catalytic performance. ACS Appl. Mater. Interfaces **5**, 12735–12743 (2013). https://doi.org/10.1021/am404123z

39. J.W. Fu, Q.L. Xu, J.X. Low, C.J. Jiang, J.G. Yu, Ultrathin 2D/2D WO$_3$/g-C$_3$N$_4$ step-scheme H$_2$ production photocatalyst. Appl. Catal. B **243**, 556–565 (2019). https://doi.org/10.1016/j.apcatb.2018.11.011

40. D.S. Lei, J.Q. Xue, X.Y. Peng, S.H. Li, Q. Bi, C.B. Tang, L. Zhang, Oxalate enhanced synergistic removal of chromium(VI) and arsenic(III) ov-er ZnFe$_2$O$_4$/g-C$_3$N$_4$: Z-scheme charge transfer pathway and photo-Fenton li-ke reaction. Appl. Catal. B **282**, 119578 (2021). https://doi.org/10.1016/j.apcatb.2020.119578

41. S. Patnaik, K.K. Das, A. Mohanty, K. Parida, Enhanced photo catalytic reduction of Cr (VI) over polymer-sensitized g-C$_3$N$_4$/ZnFe$_2$O$_4$ and its synergism with phenol oxidation

under visible light irradiation. Catal. Today **315**, 52–66 (2018). https://doi.org/10.1016/j.cattod.2018.04.008

42. Z.R. Dai, Y. Zhen, Y.S. Sun, L. Li, D.X. Ding, ZnFe$_2$O$_4$/g-C$_3$N$_4$ S-sch-eme photocatalyst with enhanced adsorption and photocatalytic activity for uranium(VI) removal. Chem. Eng. J. **415**, 129002 (2021). https://doi.org/10.1016/j.cej.2021.129002

43. Y. Guo, Y.H. Ao, P.F. Wang, C. Wang, Mediator-free direct dual-Z-scheme Bi$_2$S$_3$/BiVO$_4$/MgIn$_2$S$_4$ composite photocata-lysts with enhanced visible-li-ght-driven performance towards carbamazepine degradation. Appl. Catal. B **254**, 479–490 (2019). https://doi.org/10.1016/j.apcatb.2019.04.031

44. C.Y. Jin, C.H. Xu, W.X. Chang, X.Y. Ma, X.Y. Hu, E.Z. Liu, J. Fan, Bimetallic phosphide NiCoP anchored g-C$_3$N$_4$ nanosheets for efficient photocatalytic H$_2$ evolution. J. Alloys Compd. **803**, 205–215 (2019). https://doi.org/10.1016/j.jallcom.2019.06.252

45. Y.M. Hunge, M.A. Mahadik, R.N. Bulakhe, S.P. Yadav, J.J. Shim, A.V. Moholkar, C.H. Bhosale, Oxidative degradation of benzoic acid using spray deposited WO$_3$/TiO$_2$ thin films. J. Mater. Sci. **28**, 17976–17984 (2017). https://doi.org/10.1007/s10854-017-7740-6

46. X. Bai, Y.Y. Du, X.Y. Hu, Y.D. He, C.L. He, E.Z. Liu, J. Fan, Synergy removal of Cr (VI) and organic pollutants over RP-MoS$_2$/rGO photocatalyst. Appl. Catal. B **239**, 204–213 (2018). https://doi.org/10.1016/j.apcatb.2018.08.016

47. Y.M. Hunge, A.A. Yadav, S.W. Kang, S.J. Lim, H. Kim, Visible light activated MoS$_2$/ZnO composites for photocat-alytic degradation of ciprofloxacin antibiotic and hydrogen production. J. Photochem. Photobiol. A **434**, 114250 (2023). https://doi.org/10.1016/j.jphotochem.2022.114250

48. X.J. Chen, Y.Z. Dai, J. Guo, T.H. Liu, X.Y. Wang, Novel magneticall-y separable reduced graphene oxide (RGO)/ZnFe$_2$O$_4$/Ag$_3$PO$_4$ nanocomposite-s for enhanced photocat-alytic performance toward 2,4-Dichlorophenol under visible light. Ind. Eng. Chem. Res. **55**, 568–578 (2016). https://doi.org/10.1021/acs.iecr.5b03690

49. Z. Li, Y.N. Ma, X.Y. Hu, E.Z. Liu, J. Fan, Enhanced photo-catalytic H$_2$ production over dual-cocatalyst-modified g-C$_3$N$_4$ heterojunctions. Chin. J. Catal. **40**, 434–445 (2019). https://doi.org/10.1016/S1872-2067(18)63189-4

50. K.L. He, J. Xie, Z.Q. Liu, N. Li, X.B. Chen, J. Hu, X. Li, Multi-functional Ni$_3$C cocatalyst/g-C$_3$N$_4$ nanoheterojunctions for robust photocatalytic H$_2$ evolution under visible light. J. Mater. Chem. A **6**, 13110–13122 (2018). https://doi.org/10.1039/c8ta03048k

51. K. Wang, Y. Li, J. Li, G.K. Zhang, Boosting interfacial charge separation of Ba$_5$Nb$_4$O$_{15}$/g-C$_3$N$_4$ photocatalysts by 2D/2D nanojunction towards efficient visible-light driven H$_2$

generation. Appl. Catal. B **263**, 117730 (2020). https://doi.org/10.1016/j.apcatb.2019.05.032

52. D.S. Lei, J.Q. Xue, Q. Bi, C.B. Tang, L. Zhang, 3D/2D direct Z-schem-e photocatalyst Zn$_2$SnO$_4$/CdS for simultaneous removal of Cr(VI) and orga-nic pollutant. Appl. Surf. Sci. **517**, 146030 (2020). https://doi.org/10.1016/j.apsusc.2020.146030

53. Y.M. Hunge, A.A. Yadav, S.W. Kang, B.M. Mohite, Role of nanotechnology in photocatalysis application. Recent Pat. Nanotechnol. **17**, 5–7 (2023). https://doi.org/10.2174/1872210516666220304162429

54. X.D. Yang, J. Duan, X. Zhang, H.Y. Zhang, X.L. Liu, Y.Q. Feng, M.S. Zheng, Heterojunction architecture of Nb$_2$O$_5$/g-C$_3$N$_4$ for enhancing photocatalytic activity to degrade organic pollutants and deactivate bacteria in water. Chin. Chem. Lett. **33**, 3792–3796 (2022). https://doi.org/10.1016/j.cclet.2021.11.031

55. C.Y. Xiong, Q.F. Ren, X.Y. Liu, Z. Jin, Y. Ding, H.T. Zhu, J.P. Li, R.R. Chen, Fenton activity on RhB degradation of mag-netic g-C$_3$N$_4$/diato-mite/Fe$_3$O$_4$ composites. Appl. Surf. Sci. **543**, 148844 (2021). https://doi.org/10.1016/j.apsusc.2020.148844

56. L.B. Jiang, X.Z. Yuan, G.M. Zeng, Z.B. Wu, J. Liang, X.H. Chen, L.J. Leng, H. Wang, H. Wang, Metal-free efficient photocatalyst for stable visible-light photocatalytic degrada-tion of refractory pollutant. Appl. Catal. B **221**, 715–725 (2018). https://doi.org/10.1016/j.apcatb.2017.09.059

57. J. Di, J.X. Xia, M.X. Ji, B. Wang, S. Yin, Q. Zhang, Z.G. Chen, H. Li, Advanced photocatalytic performance of gra-phene-like BN modified BiOBr flower-like materials for the removal of pollutants and mechanism insight. Appl. Catal. B **183**, 254–262 (2016). https://doi.org/10.1016/j.apcatb.2015.10.036

58. G. Li, X.Q. Cao, N. Meng, Y.M. Huang, X.D. Wang, Y.Y. Gao, X. Li, T.S. Yang, B.L. Li, Y.Z. Zhang, X.J. Lyu, Y. Liang, Fe$_3$O$_4$ supported on water caltrop-derived biochar toward peroxymonosulfate activation for urea degradation: the key role of sulfate radical. Chem. Eng. J. **433**, 133595 (2022). https://doi.org/10.1016/j.cej.2021.133595